

A Nonparametric Approach for Estimating Three-Dimensional Fiber Orientation Distribution Functions (ODFs) in Fibrous Materials

Adam Rauff, Lucas H. Timmins, Ross T. Whitaker, *Member IEEE*, and Jeffrey A. Weiss

Abstract—Many biological tissues contain an underlying fibrous microstructure that is optimized to suit a physiological function. The fiber architecture dictates physical characteristics such as stiffness, diffusivity, and electrical conduction. Abnormal deviations of fiber architecture are often associated with disease. Thus, it is useful to characterize fiber network organization from image data in order to better understand pathological mechanisms. We devised a method to quantify distributions of fiber orientations based on the Fourier transform and the Qball algorithm from diffusion MRI. The Fourier transform was used to decompose images into directional components, while the Qball algorithm efficiently converted the directional data from the frequency domain to the orientation domain. The representation in the orientation domain does not require any particular functional representation, and thus the method is nonparametric. The algorithm was verified to demonstrate its reliability and used on datasets from microscopy to show its applicability. This method increases the ability to extract information of microstructural fiber organization from experimental data that will enhance our understanding of structure-function relationships and enable accurate representation of material anisotropy in biological tissues.

Index Terms—Fibers, Fourier Transform, Nonparametric distributions, Orientation Distribution Function (ODF).

I. INTRODUCTION

Many materials consist of one or more families of fibers with varying orientations. Examples include fabricated materials such as ceramics, concrete, glass-fiber, carbon-fiber, and polymers; plant-based biomaterials including cotton, hemp, wood, and wool; and biomaterials of human tissues such as myocardium [3], skin [4], cartilage [6], arteries [7], brain [8], ligaments [9], and tendons [10]. The organization of fibers in these materials determines both physical and mechanical properties, which are modulated by parameters such as fiber thickness, length, interconnections, ratio to ground substance, and their orientations. The orientation of fibers also contributes to various physical characteristics including directional stiffness of the material [11], conductance of electrical signals [12], diffusion of water and other soluble molecules [13], thermal conductivity [14], acoustic insulation [15], and direction of cellular growth [16].

In biological soft tissues, the fibrous architecture of constituents such as collagen and elastin are fundamental to mechanical function. In articular cartilage, collagen fibrils provide the tissue with compressive stiffness [6], and the orientation of collagen fibers is the most important structural element [17]. Myocardial muscle fibers conduct electrical signals and contract, and changes in fiber angles from apex to base result in contraction and twisting of the heart (Fig. 1a,b) [3]. In arteries, collagen and elastin fibers organize into helical structures with some dispersion to resist luminal pressure, elongation, and contraction [18]. In the brain, complex nerve fiber tracts conduct electrical signals that are activated during neural activities (Fig. 1c) [19]. Because of the fundamental importance of fiber architecture to the function of biological tissues, there is a need to quantify the characteristics of these fiber families to understand structure-function relationships and characterize changes in tissue function due to growth, aging, injury and disease. A number of specialized imaging techniques have been developed and applied for this purpose, including polarized light microscopy (PLM) [20], optical coherence tomography [21], multiphoton microscopy [22], confocal microscopy [23, 24], small angle x-ray scattering [14], serial block electron microscopy (Fig. 1d) [5, 25], and more recently, diffusion-weighted magnetic resonance imaging (MRI) [2]. Once image data are available, there is a need to quantify the geometric characteristics of the fiber organization.

The distribution of fibers at locations within these image datasets are often described using a 3D orientation distribution function (ODF), a continuous probability distribution function that maps a direction to a probability value [26]. This approach provides a compact description of the fiber families within an image volume, which lends itself to graphical display as well as quantitative evaluation. A number of different approaches have been used to obtain a 3D fiber ODF from image data including the MRI signal [27–30] – as water molecules preferentially diffuse along the direction of fibers, subsequent processing of diffusion signals from MRI [31, 32], 2D Fourier analysis [33] on three perpendicular imaging planes from microscopy [22], 2D Fourier analysis on individual z-stacks [34], the structure tensor method from image analysis [23, 24], PLM [20, 35], the vector summation method [36], and the filter bank method [37].

This work was supported in part by NIH Heart, Lung, and Blood Institute under grant F31HL154781 and R01HL131856-01A1.

All authors are with the Scientific Computing and Imaging Institute at the University of Utah, Salt Lake City, Utah 84112. A. Rauff, L. H. Timmins, and J. A. Weiss, are with the Department of Biomedical Engineering (e-mail: u1143568@utah.edu; lucas.timmins@utah.edu; jeff.weiss@utah.edu). R. T. Whitaker is with the School of Computing (e-mail: whitaker@cs.utah.edu).

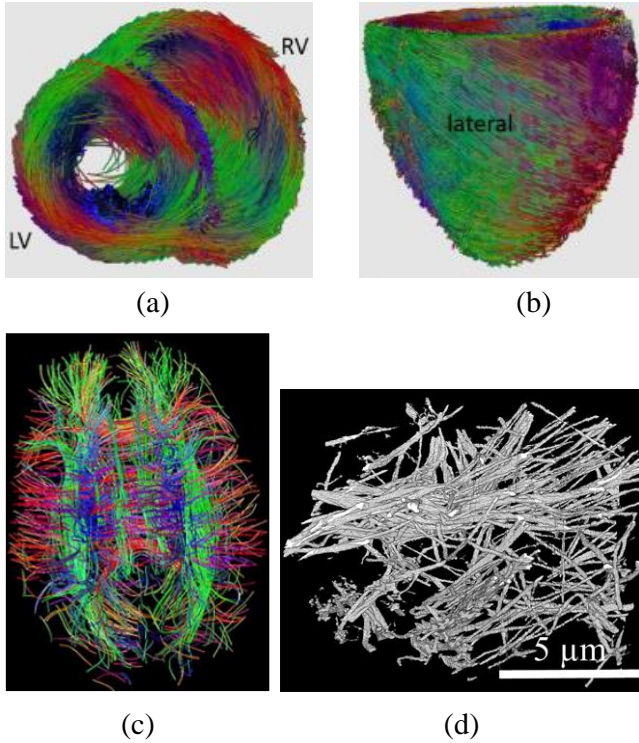


Fig. 1. Examples of fibrillar structures of biological tissues. (a-b) Muscle fibers in the heart imaged using diffusion weighted Magnetic Resonance Imaging (MRI). Images reproduced from Zhang *et al.* [1]. (a) Cardiac tissue seen from the top, with the left ventricle on the left and right ventricle on the right. (b) side view of myocardium. (c) Human brain tissue imaged using diffusion weighted MRI. Image reproduced from Hagmann *et al.* [2]. (d) Collagen fibril network imaged using scanning electron microscopy (SEM). Collagenous proteins are the most abundant structural proteins of the extracellular matrix of vertebrate organisms. Image reproduced from Reese *et al.* [5].

Despite the need to analyze 3D image data quantitatively, current approaches have significant limitations. Many approaches assume a particular parametric form for the ODF. For instance, diffusion tensor imaging of MRI assumes an underlying ellipsoidal distribution that contains six free parameters (in 3D) and has limited ability to represent crossing fibers with multiple directional preferences [29, 38]. Often, only the maximum direction and anisotropy are used for subsequent analysis. Other approaches assume the ODF can be represented by a single direction and a measure of dispersion [22, 39]. The structure tensor [23] and vector summation methods [36, 40] from image processing retain one fiber direction at each voxel. These methods, along with PLM [20], could construct an ODF by accumulating voxel-wise directions into a directional histogram. Yet, they also do not account for the errors associated with voxels that do not belong to fibers, the number of voxels in fibers, image noise, and voxels of crossing fibers. A more recent approach also quantified voxel-wise fiber directions in addition to the fiber cross-sectional area [41]. This method is similar to the vector summation method and requires costly pre-processing, in particular segmentation of the image stack. Further, our objective is to characterize physical properties of a tissue by gleaning statistical insights of the microstructures from a sub-tissue volume rather than individual voxels. To the best of our knowledge, none of these methods have implemented an objective metric of error that

compares the entire 3D approximated distributions with known ODFs.

In this study, we developed a nonparametric methodology that computes the fiber ODF from 3D images, independent of the specific imaging technology. The approach is based on the Fourier transform that decomposes a function into directional components, and the Q-ball algorithm from diffusion MRI that converts the frequency-based information to the orientation domain [42]. This provides a general-purpose algorithm for analysis of fibrous architectures in 3D images that is robust to noise, capable of high angular resolution, and is not based on predetermined distributions. It is also accompanied by an objective metric of error across ODFs based Riemannian manifolds. We demonstrated the accuracy of the algorithm using synthetic images generated from known fiber ODFs. The approximated ODF is nonparametric, as it does not assume prior knowledge about the shape of the distribution. The angular resolution of the ODF was sufficiently high to represent sharp signals such as parallel fibers, and the ability of the algorithm to resolve the details of the ODF is only limited by the image resolution and noise levels. The robustness to noise of this approach was demonstrated by adding Gaussian noise to synthetic images. Lastly, this algorithm is validated using biomedical image data from scanning electron microscopy (SEM) and lattice sheet microscopy.

II. METHODS

Fig. 2 illustrates the essential computational processes of the method introduced in this work. Volumetric images containing fibrillar structures of a material are transformed with the Fourier transform and then processed with the Q-ball algorithm. The Fourier transform decomposes a function, in this case a volumetric image, into sinusoidal basis functions. Each basis function has a unique direction, frequency, and phase. The power spectrum discards the information stored within the phase, and a further step of summation is used to discard the information on the frequency (Fig. 2b). This isolates the relative weights of the directional components of the image.

The Q-ball algorithm, originating in the literature of diffusion-weighted MRI [29] is used to resolve the fiber directions by converting the sinusoidal wave directions to their fiber orientation components (Fig. 2c). The implementation of the Q-ball utilizes a decomposition of the power spectrum to a spherical harmonic series [42], which allows for a closed-form solution to the Funk-Radon transform. The use of spherical harmonics is also advantageous for compact representation of the resultant ODF. While this results in an ODF represented by a finite number of terms, the ODF remains nonparametric as no particular distribution is assumed a priori, and the choice of the number of terms resides with the analyst and the available image resolution. The number of spherical harmonic terms determines the resolution of the approximated ODFs as higher order terms able to represent higher frequency content such as concentrated spikes in the distribution. This subject is further inspected in the results and the supplementary materials.

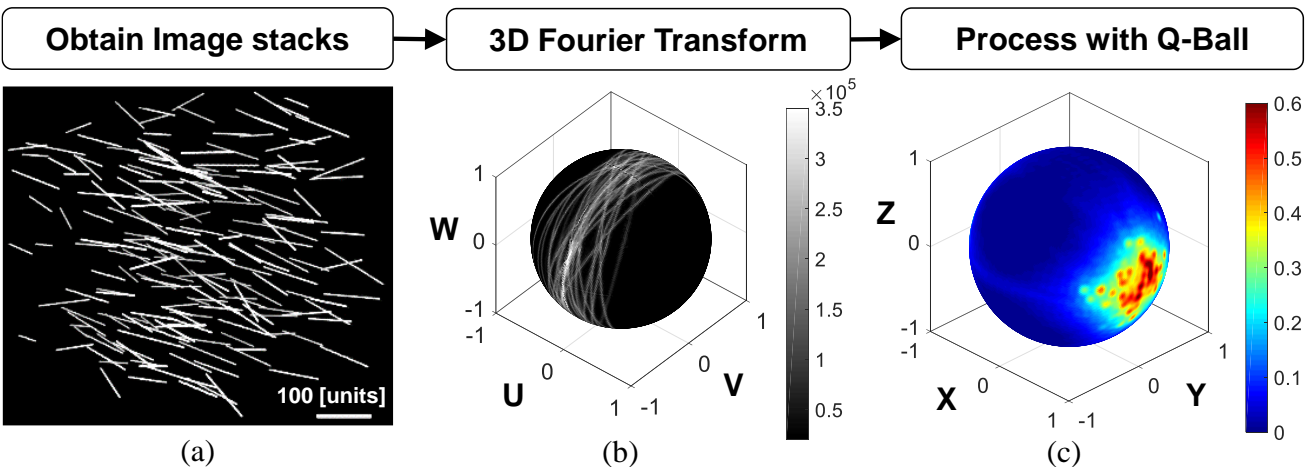


Fig. 2. Summary of algorithm. (a) Three-dimensional images are obtained using any imaging modality that can capture fibrous architecture. (b) Image is transformed with the 3D Fourier Transform, which decomposes the image into sinusoidal basis functions, each having a unique direction and wavelength. The power spectrum that is obtained from the Fourier transform is then summed along the radial direction, discarding the wavelengths but retaining the directional information. The signal in the condensed power spectrum contains relatively large amplitude perpendicular to the fiber directions. This occurs because wave-like basis functions create fiber structures when propagating perpendicular to the fiber directions. (c) The condensed power spectrum is processed with the Q-Ball algorithm, an implementation of the Funk-Radon transform that was developed in the diffusion MRI community. The Funk-Radon transform integrates the power spectrum over each great circle. This computes the amount of “signal” pointing in every direction in 3D space, and results in an orientation distribution function (ODF), as show in this panel. The ODF assigns a probability value to each direction in space, giving a statistical representation of the directions of fibers contained in the image.

A. Description of Algorithm

The methodology introduced in this paper analyzes 3D images to extract an ODF, ρ . The ODF is a probability distribution function where

$$\rho : \mathbb{S}_2 \rightarrow \mathbb{R}^+. \quad (1)$$

Here, \mathbb{S}_2 is the space of orientations, that is all unit vectors in \mathbb{R}^3 , and \mathbb{R}^+ is the space of positive scalars. The function has two constraints. The probability density distribution constraint ensures the sum of the area is one,

$$\int_0^{2\pi} \int_0^\pi \rho(\mathbf{u}) \sin \varphi d\varphi d\theta = 1, \quad (2)$$

where $\mathbf{u} \in \mathbb{S}_2$ are unit vectors denoting directions, and θ and φ are the azimuthal and polar angles. Antipodal symmetry,

$$\forall \mathbf{u}, \rho(\mathbf{u}) = \rho(-\mathbf{u}), \quad (3)$$

is a constraint that arises from the symmetrical contribution of fibers from opposing directions.

This technique utilizes the Fourier transform to extract directional components from an image using minimal pre-processing with a Butterworth filter (Supp. Mat. – Methods). The Fourier transform is used to discern the directional specificity as it decomposes the image into sinusoidal basis functions with an orientation. Images were transformed with the 3D Fourier transform to obtain $F(u, v, w)$, the frequency domain representation of the image where u , v , and w denote position within frequency domain. Next, the power spectrum, S , was computed according to the equation

$$S(u, v, w) = |F(u, v, w)|^2 = \text{Re}^2(u, v, w) + \text{Im}^2(u, v, w), \quad (4)$$

and the zero frequency was shifted to the center. S was filtered with ideal low and high pass filters to ensure the components that make up the fiber structures are included while other

components of the image, such as noise, are ignored. This was manually determined for each image set by visually checking the filtered images with the inverse Fourier transform. The image from the inverse transform was used to ensure the fibrillar structures remain while other features are attenuated. The power spectrum S was then summed along the frequencies to determine the contribution to each direction in space, and discard the wavelength information. This results in a condensed power spectrum (Fig. 2b), E , defined on the unit sphere:

$$E(\mathbf{q}_{ij}) = \sum_{u=0}^{U-1} \sum_{v=0}^{V-1} \sum_{w=0}^{W-1} S(u, v, w) \delta(1 - (\boldsymbol{\theta}_{uvw} \cdot \mathbf{q}_{ij})), \quad (5)$$

where U , V , and W , are the total number of pixels along the image dimensions, and δ denotes the Dirac delta function. The condensed power spectrum, E , is discretized as a vector quantity defined on every sampled direction \mathbf{q}_{ij} , where

$$\mathbf{q}_{ij} = [\sin(\theta_i) \cos(\varphi_j) \quad \sin(\theta_i) \sin(\varphi_j) \quad \cos(\varphi_j)]^T, \quad (6)$$

and $\boldsymbol{\theta}_{uvw}$ denotes direction of the sinusoidal basis functions obtained from the Fourier transform, where

$$\boldsymbol{\theta}_{uvw} = \frac{[u \quad v \quad w]}{\|[u \quad v \quad w]\|}. \quad (7)$$

In order to sample directions \mathbf{q}_{ij} on the unit sphere, it was discretized using N points into equal-area triangles using a tessellated icosahedron [42-44]. The condensed spectrum contains the directional components of the image in the frequency domain.

The Q-ball algorithm resolves fiber directions by converting sinusoidal wave directions to their fiber direction components. The fiber ODF was obtained by applying the Q-ball algorithm to condensed power spectra. This algorithm implements the

Funk-Radon transform that integrates over a circle perpendicular to each orientation, $\mathbf{u} \in \mathbb{S}_2$, defined by

$$\begin{aligned}\rho(\mathbf{u}) &= \int_0^{2\pi} \int_0^\pi \delta(\mathbf{u} \cdot \mathbf{q}) \mathbf{E}(\mathbf{q}) \sin \varphi d\varphi d\theta \\ &= \int_{\mathbf{q} \perp \mathbf{u}} \mathbf{E}(\mathbf{q}) d\mathbf{q}\end{aligned}. \quad (8)$$

The Funk-Radon transform was computed following the approach in Hess *et al.* and Descoteaux *et al.* [42, 44]. First, the condensed spectrum, $\mathbf{E}(\mathbf{q})$, was decomposed to a spherical harmonic series using the least squares method. A spherical harmonic series, \mathbf{Y}_l^m , is an orthogonal set of basis functions delimited by two variables, order l and phase m . This decomposition modified the harmonic bases, to have a single

index \mathbf{Y}_j , where $j := \frac{k^2 + k + 2}{2} + m$, defined by

$$\mathbf{Y}_j = \begin{cases} \sqrt{2} \operatorname{Re}(\mathbf{Y}_l^m), & -l \leq m < 0 \\ \mathbf{Y}_k^0 & . \\ \sqrt{2} \operatorname{Im}(\mathbf{Y}_l^m), & 0 \leq m < l \end{cases}. \quad (9)$$

Here, $k = 0, 2, 4, \dots, l$ is the harmonic order after re-indexing, and $m = -k, -k+1, \dots, 0, \dots, k-1, k$ is the phase after re-indexing [44]. The antipodal symmetry of ODFs means there is no information stored in odd order terms of the series (3). Then, the least squares method was used to decompose the power spectrum, \mathbf{E} , to spherical harmonic bases. The harmonic bases were represented by the matrix \mathbf{B} , defined by

$$\mathbf{B} = \begin{pmatrix} \mathbf{Y}_0(\theta_1, \varphi_1) & \dots & \mathbf{Y}_J(\theta_1, \varphi_1) \\ \vdots & \ddots & \vdots \\ \mathbf{Y}_0(\theta_N, \varphi_N) & \dots & \mathbf{Y}_J(\theta_N, \varphi_N) \end{pmatrix}. \quad (10)$$

The coefficients of the harmonic terms were stored in a vector \mathbf{c} , and the equation $\mathbf{E} = \mathbf{Bc}$ was solved using the least squares solution:

$$\mathbf{c} = (\mathbf{B}^T \mathbf{B})^{-1} \mathbf{B}^T \mathbf{E}. \quad (11)$$

Next, the closed-form solution of the Funk-Radon transform was implemented, also known as the Funk-Hecke transform

$$\rho(\mathbf{u}) = \sum_{j=1}^R 2\pi P_{l_j}(0) c_j Y_j(\mathbf{u}), \quad (12)$$

where $P_{l_j}(0)$ is a Legendre polynomial evaluated at 0 of the l^{th} degree, as defined on the j^{th} harmonic term order. The result was post-processed using a modified min-max normalization (Supp. Mat. – Methods). We have provided the Matlab code used to implement the entire processing pipeline on GitHub [45].

B. Statistical Analyses

Synthetic Fiber Image Generation. Synthetic fiber images were simulated using a custom program. The images were utilized to examine the approximation process, testing the accuracy and persistence of approximations and evaluating the robustness to noise. Synthetic images were sized at 400 cubic voxels and fibers were oriented along a user-defined underlying distribution. The image was dilated to increase the thickness of

each fiber to approximately 3 voxels, and converted to 8-bits. The exact ODF of simulated fibers was constructed by adding concentrated Gaussian functions centered on the direction of each fiber. All simulations were conducted in Matlab (Natick, MA, version 2017a). Additional information is provided in the Supplementary Materials – Methods.

Statistical Analyses of ODFs. Scalar measures are useful to summarize geometric features and apply basic statistical techniques. We utilized two scalar measures: The anisotropy of individual ODFs, and the distance between ODFs.

The anisotropy of individual ODFs was characterized by the generalized fractional anisotropy (GFA) [29]. This measure generalizes the fractional anisotropy (FA) commonly used in diffusion tensor imaging to nonparametric ODFs. Like FA, the GFA of an ODF is a scalar between zero and one that describes the degree of anisotropy, where a GFA of zero describes an isotropic distribution.

To compute the distance between ODFs, we employed an approach based on Riemannian geometry that follows Goh *et al.* [46]. Briefly, the space of ODF functions is not a vector space. This can be appreciated by considering that the addition of two ODFs does not result in a function that satisfies the probability density function constraint (2). Hence, the space of ODFs was equipped with a differential manifold structure and an inner product, that is a Riemannian manifold (Supp. Mat. – Methods). The distance metric is a value between 0° and 90° , where 0° indicates identical ODFs. The distance metric is a more sensitive measure than anisotropy as it accounts for accumulated differences across ODFs, and anisotropy is a coarser measurement that describes the shape of distributions.

C. Verification

Angular Resolution and Accuracy. The angular resolution attained by the algorithm determines the extent of high frequency content included in the approximation. This is modulated by the highest spherical harmonic order that is included, and defined by the user. The ability to approximate ODFs with high frequency content was examined by analyzing simulated images of parallel fibers, corresponding to the Dirac delta distribution. This distribution poses the greatest challenge to this approximation process because the solution consists of smooth waves. Approximating concentrated “spikes” requires high order terms, similarly required in 1D Fourier analysis. Additional analysis on the number of terms to include on experimental data was conducted using biomedical image data. ODF approximations were then compared with varying number of harmonic terms (Supp. Mat. – Methods)

Analysis of Noise. The effect of noise was assessed by adding artificial noise to simulated and experimental image datasets. A zero-mean Gaussian noise of specified variance was added to images to sample the signal to noise ratio (SNR) from 0.2 to 1.0, using an interval of 0.2, and 2.0 and 4.0. The SNR is defined as the ratio of the variance of image intensities of the noise-free image to the variance of the noisy images [47]. Approximated ODFs of images with added noise were compared to their corresponding noise-free ODFs using the scalar measures. The difference in anisotropies, measured using GFA, was used to determine significant differences. A one-way ANOVA was performed on the anisotropy differences versus

the SNR values followed by a Holm-Sidak post hoc analysis. The level of significance was set at $p = 0.05$. The analysis included harmonic orders $L = 10, 30, 40, 50$, and 70 , at each level of SNR. Another one-way ANOVA was performed on the maximum spherical harmonic order versus the distance from the noise-free approximation. All statistical tests were conducted using OriginPro (Northampton, MA, version 2021).

Algorithm Precision. The precision of this technique was determined empirically by quantifying the spread of a sample of approximated ODFs belonging to an identical underlying ODFs. This was tested by designating an exact ODF, simulating multiple images, approximating their ODFs, and comparing the spread of the approximated ODFs using the statistical measures. The “true” ODF, from which simulated fibers were generated, were oriented along the x-axis with symmetrical dispersion of $0^\circ, 1^\circ, 2^\circ, 5^\circ$, and 8° (Supp. Mat. – Figures).

D. Application to Biomedical Image Data

The algorithm was applied to experimental images to demonstrate its utility in characterizing biomaterials. The datasets were obtained from lattice light sheet microscopy and focused ion beam scanning electron microscopy [5] (Fig. 4 and 5). The lattice sheet microscopy data contained chondrocytes isolated from human articular cartilage and labelled for F-actin, while the electron microscopy data showed a network of type I collagen fibrils in a collagen hydrogel.

The dataset of the chondrocyte actin filaments exhibited highly aligned structures, and were used to demonstrate the simplicity of the technique along with a measure of validity of the approximation. The ODF was approximated and compared with the maximum probability direction computed with analysis of the moment of inertia. To obtain this auxiliary direction, the image was segmented, and the moment of inertia tensor was computed for each connected component. Then the eigenvector corresponding to the smallest eigenvalue of the inertia tensor was computed to represent the direction of each component. Next, an ODF was constructed from the moment analysis by the same procedure used for synthetic fiber generation. The direction of highest probability was then compared with the maximum direction obtained with the methodology described in this article.

The dataset of the type I collagen hydrogel contained a complex network of fibrils that vary with position. This dataset was used to demonstrate the ability to quantify material properties with spatial variation by analyzing subsets of the data. This allows quantification of the spatial variation of fiber orientations within a tissue sample.

III. RESULTS

Nonparametric fiber ODFs are directly obtained from image data without prior assumptions about the distribution. Our algorithm estimates a fiber ODF without assuming a particular parametric form or introducing directional bias (Fig. 2). Image data are transformed with the Fourier transform and the Funk-Radon transform. These well-established transforms do not introduce directional bias, as they cover the entire orientation domain. More importantly, the process does not assume any parametric form. The result is a probability distribution function on a unit sphere, which assigns a probability value to every

orientation. The orientations can be readily visualized as vectors emanating from the origin of the sphere (Fig. 2C).

Resolution of approximated ODFs depend on spherical harmonic order. The resolution of approximated fiber ODFs is determined by the number of terms in the spherical harmonic expansion. Higher order terms enable representation of increased angular resolution. This increases the accuracy of the approximated ODFs and allows for representation of functions that vary more sharply. Additionally, increased sampling of points on the unit sphere allows for higher order spherical harmonic terms to be computed, similar to discrete Fourier analysis of signals. A sampling of $N = 2,562$ points on the unit sphere afforded a maximum spherical harmonic order $L = 46$, $N = 10,242$ points allowed $L = 78$, and $N = 40,962$ points allowed $L = 84$. Approximated fiber ODF were examined with parallel fibers, which have a true ODF of the Dirac delta function (Fig. 3B). The approximated ODFs converged towards

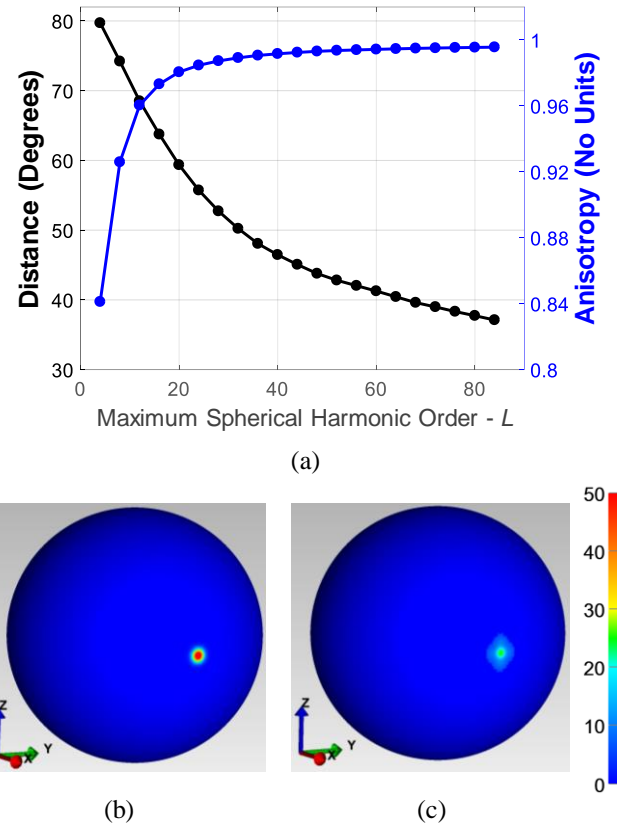


Fig. 3. Angular resolution of approximated ODFs. (a) Graph comparing approximated ODFs with increasing maximum spherical harmonic order (x-axis) to the underlying ODF (panel b). The left y-axis is the distance of the approximated ODF from the exact ODF (Methods – statistical Analysis of ODFs). The right y-axis, in blue, denotes the anisotropy of each ODF. The ODFs were approximated with a maximum spherical harmonic order $L = 6$ to 84 , and 40962 spherical sampling points. As the harmonic order increased, the distance from the exact ODF decreased monotonically. By contrast, the anisotropy increased with spherical harmonic order and tended toward a constant value of 1 . (b) Exact ODF of parallel fibers aligned along the X-axis. The green arrow stretching along the X – axis represents the direction of the fibers. (c) Approximated ODF using spherical harmonic order, $L = 84$. The general shape of the approximated ODF converges towards the true ODF, as reflected in the anisotropy and qualitatively in panels b and c. However, the approximated ODFs is not the same as the true ODF, as reflected in the distance. This is because the true ODF mostly consists of high frequency content, and this content is incrementally captured as higher order terms are added to the approximation.

the exact ODF with increasing maximum harmonic order L (Fig. 3A). The anisotropy, and the general shape, of the approximated ODFs asymptotically converged to 1 (Fig. 3A). As the spherical harmonic order was increased, the distance from the exact ODF decreased monotonically (Fig. 3A).

Number of harmonic terms to retain for experimental image data. The effect of the number of harmonic terms on experimental data was examined using biomedical images of actin filaments (Fig. 5a). ODFs were compared with the high approximation, using $L = 52$, and the “previous approximation,” of $(L - 2)$ (Supp. Fig. 1). The distance from the high order approximation, $L = 52$, decreased from 16.3° at $L = 2$ to 7.58° at $L = 6$ and 5.46° at $L = 14$. The distance from $(L - 2)$ decreased from 21.4° at $L = 4$ to 13.4° at $L = 6$ and 5.54° at $L = 8$. The change in anisotropy decreased from 0.166 at $L = 4$ to 0.01 at $L = 8$. The comparisons are graphically displayed in the supplementary materials (Supp. Mat. Fig. 1).

Effects of noise on integrity of ODF approximation. The robustness of the algorithm in the presence of noise was determined using both simulated and biomedical image data. The simulated images consisted of aligned fibers with addition of Gaussian noise to vary the signal to noise (SNR) ratio (Fig. 4b-d). Their approximated ODFs with added noise closely resembled the ODF approximated of the noise-free image. The difference between the approximated ODFs with additional noise and the noise-free ODF approximation decreased rapidly with increasing SNR, as images with $\text{SNR} \geq 1.0$ were within 2.0° of the noise-free ODF approximation (Fig. 4a). This includes ODF approximations at different spherical harmonic orders demonstrating the inclusion of higher frequency content did not corrupt the resultant ODF. The difference in anisotropies among the approximations revealed there is only a significant difference at SNR values of 0.4 and below (Supp. Mat. Fig. 2). The magnitude of the anisotropy difference was below 0.01 for all SNR values above 0.4, indicating the general shape of the ODF was similar (Supp. Mat. Fig. 2). The

biomedical image data consisted of actin filaments of a chondrocyte that were similarly corrupted with Gaussian noise (Fig. 4e-g). Their approximated ODFs with $\text{SNR} > 1.0$ were all within 0.85° of the noiseless ODF (Fig. 4a). The difference in anisotropies also revealed a significant effect at SNR values of 0.4 or below, and the difference of anisotropies above was low (<0.005), indicating similar shapes. The spherical harmonic order did not have a significant effect on the distance from the noise-free approximation.

Precision of the Algorithm. The consistency of this approach was determined by inspecting the precision of the approximation process. Synthetic fiber image data were simulated from identical underlying distributions, the “true” ODFs, and images were blurred and corrupted with noise to mimic realistic imaging conditions. The population statistics of the approximated ODFs were then analyzed to determine the consistency of the measurement. Five groups were tested of x-aligned fibers with true ODF containing symmetrical dispersion of 0° , 1° , 2° , 5° , and 8° . The average deviations from the mean ODF, indicating the precision of the approximation process, were 6.32° , 5.06° , 4.47° , 2.87° , and 2.57° respectively (Supp. Fig. 3a). The deviations from the population mean provide baseline measures to determine statistically significance differences. The standard deviation of the approximated anisotropy of each group were 0.012, 0.016, 0.018, 0.02, 0.02 respectively (Supp. Fig. 3b). Because the anisotropy is a descriptive statistic, the standard deviation of the anisotropies serves as the measure of precision.

Application to Biomedical Image Data. The utility of the algorithm was demonstrated by application to image data from lattice sheet microscopy of actin filaments in a chondrocyte, and focused ion beam SEM of a type I collagen network in a hydrogel [5]. The datasets contain filamentous structures with a clear preferred direction (Fig. 5 and 6).

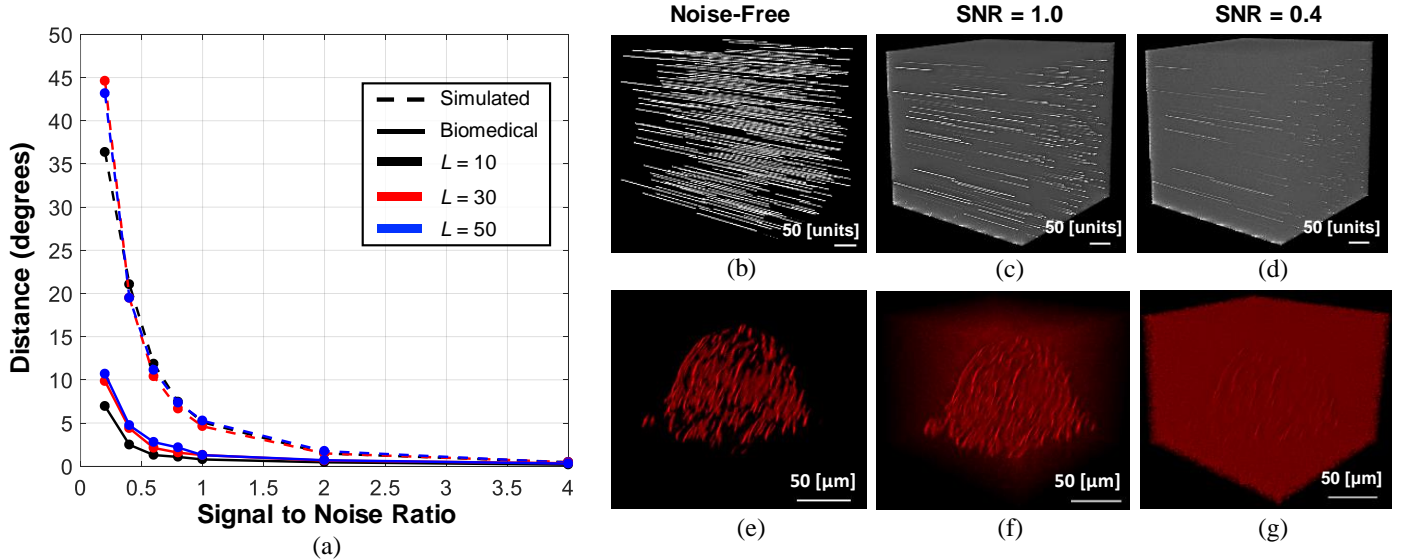


Fig. 4. Analysis of the effect of noise on approximated ODFs. (a) Graph exhibiting the distance from the noise-free ODF approximations. Image data were modified to include varying signal to noise ratios (SNR), graphed along the x axis, sampled from a minimum of 0.2 to a maximum of 4. SNR is defined as the ratio of the variance of the noise-free image to the variance of the added noise. (b - d) Simulated fibers aligned along one axis with varying SNR. As the amount of noise increases, the SNR decreases, and the image content is corrupted. (e - g) Biomedical image data of actin filaments of a chondrocyte with varying levels of SNR. The distance was measured between an image corrupted with noise at every SNR and the ODF approximation of the noise-free image.

The analysis of the actin filaments provided accurate quantitative and qualitative results (Fig. 5). As expected, the approximated ODF contains a single mode of concentrated probabilities and a high anisotropy with GFA of 0.7883 (Fig. 5b). These statistics were obtained without making any assumption about the material symmetry, the underlying form of the ODF, or the need to conduct any substantial pre-processing on the image. Furthermore, the maximum ODF direction and the direction of the principal moment of inertia were almost identical, with an angle of $8.538 \cdot 10^{-7}$ ° between the axes. In contrast to the results obtained using our algorithm, the moment of inertia analysis required time-intensive segmentation and image pre-processing.

The analysis of type I collagen made use of focused ion beam scanning electron microscopy (FIB-SEM) image data [5]. The microstructural properties of biological tissues are highly complex and vary with position (Fig. 6). Two sub-volumes from the dataset were selected to demonstrate the tissue's spatial variation of fibril orientations. The subsets consisted of 500 voxels cubed and are highlighted in green and white (Fig. 6c,e). Both ODFs displayed a single mode of preferred fiber orientation that appears to be consistent with the image data. However, one ODF approximation displays deviation from the ODF mode along a preferred plane (Fig. 6c), while the other ODF displays deviation relatively isotropic (Fig. 6e). The distance between the maximum direction of the ODFs was 57.10° and their Riemannian distance was 42.76°.

IV. DISCUSSION

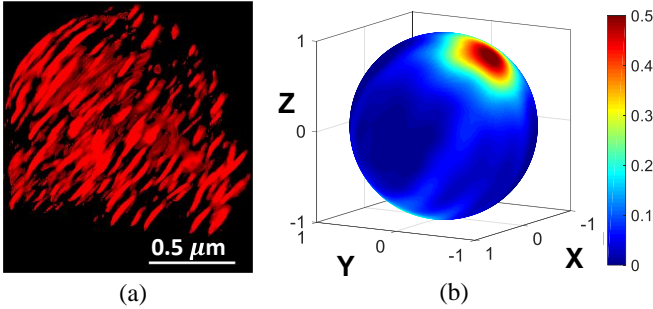


Fig. 5. Application to chondrocyte actin filaments. (a) Volume rendering of lattice sheet microscopy data of a chondrocyte stained for actin intermediate filaments. (b) Approximated ODF of the image dataset using spherical harmonic order, $L = 16$. The ODF contains a single mode of concentrated probabilities that is visually consistent with the direction of actin fibers in panel a.

This algorithm provides a straightforward approach to obtain nonparametric 3D fiber orientation distributions from image volumes. It is simple and efficient because its mathematical underpinnings are the Fourier transform and the Funk-Radon transform. This essentially decomposes an image into its rudimentary structures continuously along all orientations and counts the structures pointing along a given direction relative to all other directions. The process does not require costly pre-processing or segmentation, and provides an objective means to compare fiber ODFs. Other algorithms exist for the purpose of quantifying the orientation of fibers in 3D images, yet previous approaches contain a priori assumptions about the distribution [22], ignore orientations along the depth of the image [34], or quantify voxel-wise fiber directions [23, 36, 41] that are not optimal to capture the statistical distribution over a volume.

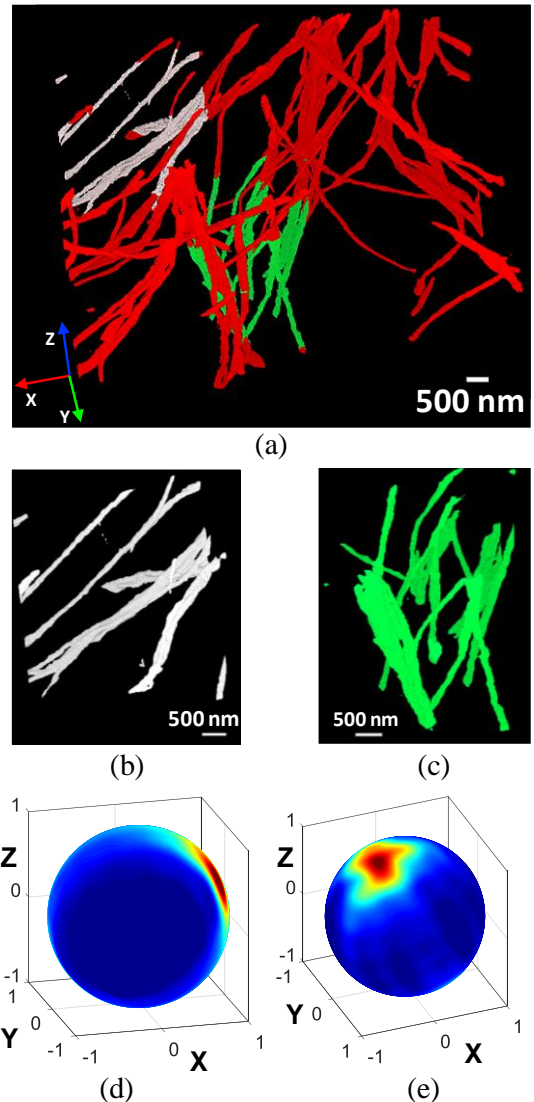


Fig. 6. Application to biomedical image data of scanning electron microscopy images of a type I collagen hydrogel. (a) Volume rendering of the microscopy data of seen in red. Two subvolumes of 500 voxels cubed are displayed in white and green. (b) Expanded view of the subvolume displayed in white. (c) Expanded view of the green subvolume. (d) Approximated orientation distribution function (ODF) of the subvolume exhibited in panel b using maximum spherical harmonic order, $L = 16$. (e) Approximated ODF of the subvolume exhibited in panel c using maximum spherical harmonic order, $L = 16$. The two ODFs had a distance of 42.76°, indicating they are different.

Examining approaches that have been used for the extraction of fiber orientation from 2D images can offer an insight into the utility of multiple methods. Several methods for 2D analysis exist and are regularly used in a field-specific manner. For example fabric tensors in cancellous bone [48, 49], the line fraction deviation used on bone microstructures [50, 51], and Fourier transform-based methods used with collagen fibrils, cell alignment, and textiles [52-54]. The Fourier transform based methods have emerged as the most reliable in capturing the anisotropy and orientation distribution and are the fastest and most accurate [50]. Our proposed methodology generalizes the utilities of the 2D technique to 3D analysis.

Our approach was rigorously tested to enable adoption amongst experimental scientists. The accuracy of the resultant ODF was determined with respect to the Dirac delta

distribution. This true ODF presents the most extreme possibility of high frequency content that would be a challenge to estimate using this processing pipeline since our solution consists of smooth waves. The precision of the approach was measured by empirical means and depends on the nature of the underlying, true ODF. The analysis utilized highly aligned fibril configurations and further analysis is needed to rigorously quantify the precision. Notwithstanding, the results provide an indication of the consistency and serve as practical guidance for determining confidence in measurements. Moreover, the approach was applied to experimental image data of actin filaments to provide some quantitative verification of the approximated ODF. The result was assessed relative to the principal moment of inertia, which only measures the preferred direction. Experimental data are difficult to validate as the underlying ODF is unknown, and there is no gold standard technique for extraction 3D fiber ODFs from volumetric images. Nevertheless, the analysis with biomedical image data show the technique can be effectively used to obtain experimentally derived fiber ODFs. These tests, along with the simplicity of the algorithm and its utility, will enable straightforward adoption by experimental scientists and yield more specific data about tissues' microstructural organization.

The Riemannian metric provides a scalar metric to compare ODFs objectively. This enables objective quantification of experimental differences that will lead to clear diagnostic standards amongst fibrillar structures deviating from physiologic ranges. In addition, this metric may be useful in optimization tasks and spatial interpolation for biophysical modeling. The objective nature of the metric affords the capability to compute a mean and variance from a sample of ODFs (Supp. Mat. – Fig. 3), interpolation between spatial locations of measurement [46], and a framework for infinitesimal perturbations that could be used in optimization routines such as synthetic fabrication of soft tissues with designated mechanical criteria.

The approximated ODFs provide structural characteristics inside a given volume that are indicators of physical properties of materials. These attributes may dictate stiffness, diffusivity, electrical conduction, and other physical properties. This is of particular interest in biological tissues, where the information could advance our knowledge of tissue function and dysfunction during age, growth, injury, and disease.

The fiber ODFs that can be quantified using the approach in this paper are useful in constitutive modeling of materials. Prior studies incorporating experimentally derived fiber orientations involved assumptions about the form of the probability distribution, such as ellipsoidal or Von-Mises [18, 22], or ignored fibers with orientations along the depth of an image stack [34]. However, constitutive formulations that incorporate distributions of fibers do not require a specific form of distribution. In fact, nonparametric ODFs can readily be incorporated with existing strain energy formulations. The algorithm developed in the present research provides the framework to derive highly complex ODFs directly from image data and use them as input to constitutive models of materials. The spherical harmonic representation allows a concise representation of orientation distributions that can be used to store the probability densities for every direction at a given

volumetric element of a material. Incorporating these ODFs will refine the structural information and increase constitutive specificity to further advance structural approaches.

3D fiber orientations are also of interest in other fields of study including diffusion in a porous medium, cellular growth inside tissues, and electrical conduction in neuronal pathways and muscle tissues. Biological tissues are porous media, where water comprises the highest percentage by weight and volume, and transport of molecules through the fibrillar matrix is an important mode of biological activity [55, 56]. The quantification of fiber ODFs from microscopic images to validate diffusion MRI data has been sought as it provides a comparison of data across imaging modalities [20, 23]. The spatial distribution of diffusivity is important to the functions of tissues in health and disease, and an anisotropic distribution of fibers is associated with anisotropic diffusion profile [57, 58]. Further, the local fiber arrangement provides attachment sites to cells during migration and growth, acting as a contact guidance mechanisms that modulates cellular phenotypes and intracellular signaling [59, 60]. The conduction of electrical signals is of particular interest in myocardial and nerve tissues. The myocardium contains muscle fibers that vary in orientation to enable the heart to contract and twist during systole [3]. The muscle fibers act as both contractile and conductive units. Similarly, neural pathways also act as conductive units, among other functions, to carry signals for the body's motor systems, and within specific pathways within the brain.

The study has several limitations. The images under analysis need to contain an equal number of pixels along the height, width, and depth. This ensures there is no bias in the directions presented in the power spectrum, and the same frequencies are present in all directions. Further, the aspect ratio of voxels also needs to be isotropic to ensure there is no directional bias. Both of these limitations are inherent in the use of the 3D FFT method, regardless of the application. However, the size of the image and the voxel aspect ratio may be adjusted by use of resampling or selection of regions of interest.

The filtering of the power spectrum is determined by the analyst, introducing some subjectivity. This feature of Fourier transform-based methods enables simple application to complex experimental data to gain reasonably accurate results. It is also the reason Fourier transform methods have become so wide-spread and effective compared with other methods [50]. While there is some inherent subjectivity to this stage of processing, there are guiding principles. The impact on the original image can be observed with an inverse transform, allowing visual inspection after filtering. As a starting point, the frequencies pertaining to twice the average fiber cross section diameter plus or minus 10% should be isolated [61]. Guidance for use of user-determined variables involved in this technique are summarized in Table 1 of the Supplementary Materials.

The spherical harmonic decomposition utilized the least squares method [42] and more efficient harmonic decomposition algorithms have been published [62]. Use of these more efficient methods could allow greater angular resolution with decreased computations and memory. However, this process currently runs on images up to 700^3 voxels while retaining terms up to the 84th harmonic order, on a desktop CPU where the computational time was approximately 2.5

hours using $N = 40,962$ sampling points without substantial parallelization. As an example of a more reasonable approximation, the actin filaments dataset (Fig. 5) was processed in 13.01 seconds using $L = 18$ and $N = 40,962$.

Estimation of fiber ODFs is likely to result in some blurring. The approximation depends on decomposition of the image into waves of varying wavelengths. Spurious signal or sharp edges in the ODF will be smoothed. We have employed post-processing on the ODF to ensure the low frequencies are anchored at zero (Supp. Mat. – Methods). This is a crude measure to undo some of the deterministic underperformance of this method. This approach needs to be further studied and refined to ensure there is no loss of information. Additionally, this has been remedied in the MRI literature by applying spherical deconvolution to sharpen the ODF signal [32].

ACKNOWLEDGMENT

We acknowledge financial support from NIH F31HL154781 awarded to A.R and NIH R01HL131856 awarded to J.A.W. We thank Dr. Sarang Joshi for his assistance with the mathematical background for the analysis of ODFs. We thank Dr. Scott Wood, for the chondrocyte cultures and imaging and the double-transfection technique used for labelling. Lastly, we thank Dr. Jared Zitnay for his insightful conversations and constructive critique.

REFERENCES

- [1] Y. Zhang and H. Wei, "Atlas construction of cardiac fiber architecture using a multimodal registration approach," *Neurocomputing*, vol. 259, pp. 219-225, 2017/10/11/ 2017.
- [2] P. Hagmann, L. Jonasson, P. Maeder, J.-P. Thiran, V. J. Wedeen, and R. Meuli, "Understanding diffusion MR imaging techniques: from scalar diffusion-weighted imaging to diffusion tensor imaging and beyond," *Radiographics*, vol. 26, pp. S205-S223, 2006.
- [3] D. D. Streeter Jr, H. M. Spotnitz, D. P. Patel, J. Ross Jr, and E. H. Sonnenblick, "Fiber orientation in the canine left ventricle during diastole and systole," *Circulation research*, vol. 24, pp. 339-347, 1969.
- [4] Y. Lanir, "The fibrous structure of the skin and its relation to mechanical behaviour," in *Bioengineering and the skin*, ed: Springer, 1981, pp. 93-95.
- [5] S. P. Reese, N. Farhang, R. Poulson, G. Parkman, and J. A. Weiss, "Nanoscale imaging of collagen gels with focused ion beam milling and scanning electron microscopy," *Biophysical journal*, vol. 111, pp. 1797-1804, 2016.
- [6] V. C. Mow and R. Huiskes, *Basic orthopaedic biomechanics & mechanobiology*: Lippincott Williams & Wilkins, 2005.
- [7] P. B. CANHAM, H. M. FINLAY, J. G. DIXON, D. R. BOUGHNER, and A. CHEN, "Measurements from light and polarised light microscopy of human coronary arteries fixed at distending pressure," *Cardiovascular research*, vol. 23, pp. 973-982, 1989.
- [8] V. J. Wedeen, D. L. Rosene, R. Wang, G. Dai, F. Mortazavi, P. Hagmann, J. H. Kaas, and W.-Y. I. Tseng, "The geometric structure of the brain fiber pathways," *Science*, vol. 335, pp. 1628-1634, 2012.
- [9] P. P. Provenzano and R. Vanderby Jr, "Collagen fibril morphology and organization: implications for force transmission in ligament and tendon," *Matrix Biology*, vol. 25, pp. 71-84, 2006.
- [10] P. Kannus, "Structure of the tendon connective tissue," *Scandinavian journal of medicine & science in sports*, vol. 10, pp. 312-320, 2000.
- [11] Y. Lanir, "Constitutive equations for fibrous connective tissues," *Journal of biomechanics*, vol. 16, pp. 1-12, 1983.
- [12] M. Neunlist and L. Tung, "Spatial distribution of cardiac transmembrane potentials around an extracellular electrode: dependence on fiber orientation," *Biophysical journal*, vol. 68, pp. 2310-2322, 1995.
- [13] T. Stylianopoulos, B. Diop-Frimpong, L. L. Munn, and R. K. Jain, "Diffusion Anisotropy in Collagen Gels and Tumors: The Effect of Fiber Network Orientation," *Biophysical journal*, vol. 99, pp. 3119-3128, 2010/11/17/ 2010.
- [14] N. Pan and P. Gibson, *Thermal and moisture transport in fibrous materials*: Woodhead Publishing, 2006.
- [15] X. Lu and M. Viljanen, "10 - Fibrous insulation materials in building engineering applications," in *Fibrous and Composite Materials for Civil Engineering Applications*, R. Fangueiro, Ed., ed: Woodhead Publishing, 2011, pp. 271-305.
- [16] R. J. Petrie, A. D. Doyle, and K. M. Yamada, "Random versus directionally persistent cell migration," *Nature reviews Molecular cell biology*, vol. 10, p. 538, 2009.
- [17] J. C. Mansfield, C. P. Winlove, J. J. Moger, and S. J. Matcher, "Collagen fiber arrangement in normal and diseased cartilage studied by polarization sensitive nonlinear microscopy," *Journal of biomedical optics*, vol. 13, p. 044020, 2008.
- [18] T. C. Gasser, R. W. Ogden, and G. A. Holzapfel, "Hyperelastic modelling of arterial layers with distributed collagen fibre orientations," *Journal of the royal society interface*, vol. 3, pp. 15-35, 2005.
- [19] M. Lazar, "Mapping brain anatomical connectivity using white matter tractography," *NMR in biomedicine*, vol. 23, pp. 821-835, 2010.
- [20] M. Axer, S. Strohmer, D. Gräsel, O. Bücker, M. Dohmen, J. Reckfort, K. Zilles, and K. Amunts, "Estimating fiber orientation distribution functions in 3D-polarized light imaging," *Frontiers in neuroanatomy*, vol. 10, p. 40, 2016.
- [21] N. Uglyumova, S. V. Gangnus, and S. J. Matcher, "Three-dimensional optic axis determination using variable-incidence-angle polarization-optical coherence tomography," *Optics letters*, vol. 31, pp. 2305-2307, 2006.
- [22] M. B. Lilledahl, D. M. Pierce, T. Ricken, G. A. Holzapfel, and C. de Lange Davies, "Structural analysis of articular cartilage using multiphoton microscopy: input for biomechanical modeling," *IEEE transactions on medical imaging*, vol. 30, pp. 1635-1648, 2011.
- [23] K. Schilling, V. Janve, Y. Gao, I. Stepniewska, B. A. Landman, and A. W. Anderson, "Comparison of 3D orientation distribution functions measured with confocal microscopy and diffusion MRI," *Neuroimage*, vol. 129, pp. 185-197, 2016.
- [24] A. R. Khan, A. Cornea, L. A. Leigland, S. G. Kohama, S. N. Jespersen, and C. D. Kroenke, "3D structure tensor analysis of light microscopy data for validating diffusion MRI," *Neuroimage*, vol. 111, pp. 192-203, 2015.
- [25] T. Starborg, N. S. Kalson, Y. Lu, A. Mironov, T. F. Coates, D. F. Holmes, and K. E. Kadler, "Using transmission electron microscopy and 3View to determine collagen fibril size and three-dimensional organization," *Nature protocols*, vol. 8, p. 1433, 2013.
- [26] K. V. Mardia and P. E. Jupp, *Directional statistics* vol. 494: John Wiley & Sons, 2009.
- [27] P. J. Basser, J. Mattiello, and D. LeBihan, "MR diffusion tensor spectroscopy and imaging," *Biophysical journal*, vol. 66, pp. 259-267, 1994.
- [28] D. M. Pierce, M. J. Unterberger, W. Trobin, T. Ricken, and G. A. Holzapfel, "A microstructurally based continuum model of cartilage viscoelasticity and permeability incorporating measured statistical fiber orientations," *Biomechanics and modeling in mechanobiology*, vol. 15, pp. 229-244, 2016.
- [29] D. S. Tuch, "Q-ball imaging," *Magnetic Resonance in Medicine: An Official Journal of the International Society for Magnetic Resonance in Medicine*, vol. 52, pp. 1358-1372, 2004.
- [30] V. J. Wedeen, P. Hagmann, W. Y. I. Tseng, T. G. Reese, and R. M. Weisskoff, "Mapping complex tissue architecture with diffusion spectrum magnetic resonance imaging," *Magnetic resonance in medicine*, vol. 54, pp. 1377-1386, 2005.
- [31] J.-D. Tournier, F. Calamante, D. G. Gadian, and A. Connelly, "Direct estimation of the fiber orientation density function from diffusion-weighted MRI data using spherical deconvolution," *Neuroimage*, vol. 23, pp. 1176-1185, 2004.
- [32] J.-D. Tournier, F. Calamante, and A. Connelly, "Robust determination of the fibre orientation distribution in diffusion MRI: non-negativity constrained super-resolved spherical deconvolution," *Neuroimage*, vol. 35, pp. 1459-1472, 2007.
- [33] B. Josso, D. R. Burton, and M. J. Lalor, "Texture orientation and anisotropy calculation by Fourier transform and principal component analysis," *Mechanical Systems and Signal Processing*, vol. 19, pp. 1152-1161, 2005.
- [34] A. J. Schriefl, H. Wolinski, P. Regtnig, S. D. Kohlwein, and G. A. Holzapfel, "An automated approach for three-dimensional quantification

- of fibrillar structures in optically cleared soft biological tissues," *Journal of the royal society interface*, vol. 10, p. 20120760, 2013.
- [35] M. Axer, K. Amunts, D. Grassel, C. Palm, J. Dammers, H. Axer, U. Pietrzyk, and K. Zilles, "A novel approach to the human connectome: ultra-high resolution mapping of fiber tracts in the brain," *Neuroimage*, vol. 54, pp. 1091-101, Jan 15 2011.
- [36] Z. Liu, K. P. Quinn, L. Speroni, L. Arendt, C. Kuperwasser, C. Sonnenschein, A. M. Soto, and I. Georgakoudi, "Rapid three-dimensional quantification of voxel-wise collagen fiber orientation," *Biomed Opt Express*, vol. 6, pp. 2294-310, Jul 1 2015.
- [37] T. Y. Lau, R. Ambekar, and K. C. Toussaint, "Quantification of collagen fiber organization using three-dimensional Fourier transform-second-harmonic generation imaging," *Optics express*, vol. 20, pp. 21821-21832, 2012.
- [38] M. R. Wiegell, H. B. Larsson, and V. J. Wedeen, "Fiber crossing in human brain depicted with diffusion tensor MR imaging," *Radiology*, vol. 217, pp. 897-903, 2000.
- [39] T. Y. Lau, R. Ambekar, and K. C. Toussaint, "Quantification of collagen fiber organization using three-dimensional Fourier transform-second-harmonic generation imaging," *Opt Express*, vol. 20, pp. 21821-32, Sep 10 2012.
- [40] Z. Liu, D. Pouli, D. Sood, A. Sundarakrishnan, C. K. Hui Mingalone, L. M. Arendt, C. Alonzo, K. P. Quinn, C. Kuperwasser, L. Zeng, T. Schnelldorfer, D. L. Kaplan, and I. Georgakoudi, "Automated quantification of three-dimensional organization of fiber-like structures in biological tissues," *Biomaterials*, vol. 116, pp. 34-47, 2017/02/01/ 2017.
- [41] J. D. Eekhoff and S. P. Lake, "Three-dimensional computation of fibre orientation, diameter and branching in segmented image stacks of fibrous networks," *Journal of the royal society interface*, vol. 17, p. 20200371, 2020.
- [42] C. P. Hess, P. Mukherjee, E. T. Han, D. Xu, and D. B. Vigneron, "Q-ball reconstruction of multimodal fiber orientations using the spherical harmonic basis," *Magnetic Resonance in Medicine: An Official Journal of the International Society for Magnetic Resonance in Medicine*, vol. 56, pp. 104-117, 2006.
- [43] A. Semechko, "Suite of functions to perform uniform sampling of a sphere ", ed. GitHub, 2019.
- [44] M. Descoteaux, E. Angelino, S. Fitzgibbons, and R. Deriche, "Regularized, fast, and robust analytical Q-ball imaging," *Magnetic Resonance in Medicine: An Official Journal of the International Society for Magnetic Resonance in Medicine*, vol. 58, pp. 497-510, 2007.
- [45] A. Rauff. (2021, August). *FiberODF* (1 ed.) [Github Repository]. Available: <https://github.com/AdamRauff/FiberODF>
- [46] A. Goh, C. Lenglet, P. M. Thompson, and R. Vidal, "A nonparametric Riemannian framework for processing high angular resolution diffusion images (HARDI)," in *2009 IEEE Conference on Computer Vision and Pattern Recognition*, 2009, pp. 2496-2503.
- [47] A. I. Veress, G. T. Gullberg, and J. A. Weiss, "Measurement of strain in the left ventricle during diastole with cine-MRI and deformable image registration," 2005.
- [48] Z. Tabo and E. Rokita, "Quantifying anisotropy of trabecular bone from gray-level images," *Bone*, vol. 40, pp. 966-972, 2007.
- [49] S. C. Cowin, "The relationship between the elasticity tensor and the fabric tensor," *Mechanics of Materials*, vol. 4, pp. 137-147, 1985.
- [50] E. A. Sander and V. H. Barocas, "Comparison of 2D fiber network orientation measurement methods," *Journal of Biomedical Materials Research Part A: An Official Journal of The Society for Biomaterials, The Japanese Society for Biomaterials, and The Australian Society for Biomaterials and the Korean Society for Biomaterials*, vol. 88, pp. 322-331, 2009.
- [51] W. Geraets, "Comparison of two methods for measuring orientation," *Bone*, vol. 23, pp. 383-388, 1998.
- [52] S. Chaudhuri, H. Nguyen, R. M. Rangayyan, S. Walsh, and C. B. Frank, "A Fourier domain directional filtering method for analysis of collagen alignment in ligaments," *IEEE transactions on biomedical engineering*, pp. 509-518, 1987.
- [53] B. Palmer and R. Bizios, "Quantitative characterization of vascular endothelial cell morphology and orientation using Fourier transform analysis," 1997.
- [54] B. Pourdeyhimi, R. Dent, and H. Davis, "Measuring fiber orientation in nonwovens part III: Fourier transform," *Textile Research Journal*, vol. 67, pp. 143-151, 1997.
- [55] O. Boubriak, J. Urban, S. Akhtar, K. Meek, and A. J. Bron, "The effect of hydration and matrix composition on solute diffusion in rabbit sclera," *Experimental eye research*, vol. 71, pp. 503-514, 2000.
- [56] X. Lu and V. Mow, "Biomechanics of articular cartilage and determination of material properties," *Medicine+ Science in Sports+ Exercise*, vol. 40, p. 193, 2008.
- [57] L. Filidoro, O. Dietrich, J. Weber, E. Rauch, T. Oerther, M. Wick, M. Reiser, and C. Glaser, "High-resolution diffusion tensor imaging of human patellar cartilage: feasibility and preliminary findings," *Magnetic Resonance in Medicine: An Official Journal of the International Society for Magnetic Resonance in Medicine*, vol. 53, pp. 993-998, 2005.
- [58] C. Pierpaoli, P. Jezzard, P. J. Basser, A. Barnett, and G. Di Chiro, "Diffusion tensor MR imaging of the human brain," *Radiology*, vol. 201, pp. 637-648, 1996.
- [59] D. G. Brownfield, G. Venugopalan, A. Lo, H. Mori, K. Tanner, D. A. Fletcher, and M. J. Bissell, "Patterned collagen fibers orient branching mammary epithelium through distinct signaling modules," *Current biology*, vol. 23, pp. 703-709, 2013.
- [60] E. S. Lai, N. F. Huang, J. P. Cooke, and G. G. Fuller, "Aligned nanofibrillar collagen regulates endothelial organization and migration," *Regenerative medicine*, vol. 7, pp. 649-661, 2012.
- [61] J. P. Marquez, "Fourier analysis and automated measurement of cell and fiber angular orientation distributions," *International Journal of Solids and Structures*, vol. 43, pp. 6413-6423, 2006/10/01/ 2006.
- [62] Z. Khalid, R. A. Kennedy, and J. D. McEwen, "An optimal-dimensionality sampling scheme on the sphere with fast spherical harmonic transforms," *IEEE Transactions on Signal Processing*, vol. 62, pp. 4597-4610, 2014.